

A finite element model with refined enrichment for boundary layers in glass cooling

M. Shadi Mohamed*, Mohammed Seaid†, Jon Trevelyan†, Omar Laghrouche*

Abstract

We investigate the effectiveness of the partition-of-unity method for the numerical resolution of thermal boundary layers in glass cooling problems. The governing equations consist of a semi-linear transient heat equation for the temperature field and a stationary diffusion approximation to the radiation in non-grey semitransparent media. The coupled equations are integrated in time using a semi-implicit method in the finite element framework. We show that for the considered problems, a class of exponential enrichment functions based on an approximation of the boundary layer leads to improved accuracy, for a prescribed model size, compared to the conventional finite element method. It is illustrated that this approach can be more efficient than using h adaptivity to increase the accuracy of the finite element method near the medium walls. The performance of the proposed method is analysed for glass cooling of two enclosures in frequency-dependent media.

Keywords. Finite-element method; Partition-of-unity method; Radiative heat transfer problems; Simplified P_1 approximation; Glass cooling

Nomenclature

| | |
|---------------|--|
| ρ | density, ($kg.m^{-3}$) |
| c | specific heat capacity, ($J.kg^{-1}K^{-1}$) |
| ϵ | emissitivity |
| ϱ | reflectivity |
| κ | absorption coefficient, (m^{-1}) |
| λ | heat conduction coefficient, ($W.m^{-1}K^{-1}$) |
| h | convective heat transfer coefficient, ($W.m^{-1}K^{-1}$) |
| ν | frequency variable, (μm^{-1}) |
| ε | diffusion scaling |
| Ω | angular direction |
| I | radiative intensity, ($J.m^{-2}\mu m$) |
| φ | mean radiative intensity, ($J.m^{-2}$) |
| T | temperature, (K) |

*School of the Built Environment, Heriot Watt University, Edinburgh EH14 4AS, UK

†School of Engineering and Computing Sciences, University of Durham, South Road, Durham DH1 3LE, UK

| | |
|-----------------------|---|
| B | Planck function, ($W.m^{-2}\mu m^{-1}$) |
| T_b | surround medium temperature, (K) |
| T_0 | initial temperature, (K) |
| n_{glass} | refractive index of glass |
| n_b | refractive index of surrounding medium |
| t | time, (s) |
| \mathbf{x} | spatial coordinate, (m) |
| \mathcal{D} | spatial domain |
| $\partial\mathcal{D}$ | domain boundary |
| S^2 | unit sphere |
| \mathbf{n} | surface normal |

1 Introduction

Heat transfer phenomena involve different mechanisms such as thermal conduction, convection and radiation. The first two mechanisms are the most commonly considered in heat transfer simulations while the thermal radiation is often neglected because of (i) the high computational cost, and (ii) the uncertainty related to the optical properties of the materials being modelled. Another complexity is related to the complicated physical models which need to be solved in order to consider thermal radiation. The computational cost involved in considering thermal radiation is mainly caused by the wide spectrum of electromagnetic waves that are emitted from a thermally radiating material. The optical properties of this material defines the active frequencies through which most of the heat energy radiates. The model describing the thermal radiation needs to be solved for each of these frequency bands in order to estimate the cumulative heat energy emitted through radiation. The change in the heat energy through different mechanisms results in a change in the material temperature. Hence, the new temperature needs to be accounted for when considering these mechanisms in the time domain. Acting in the time domain the thermal radiation adds an extra complexity to other heat transfer mechanisms. The radiation waves move at the light speed whereas other mechanisms happen at a much larger time scales. Thus the radiation scale has an effect on the scale used in the solution of other coupled mechanisms [?, ?].

Although it may be possible in some cases to neglect it, Radiative Heat Transfer (RHT) has important applications in engineering and science: nuclear power plants [?], turbojet engines [?] and thermal management in space [?] are only a few examples where ignoring the RHT can introduce a significant error [?]. In the full simulation of RHT systems, the radiative transfer, which is an integro-differential equation, must be solved along with the partial differential equations of material, momentum, energy transport and chemical reactions as a fully coupled system [?]. The most accurate procedures available in the literature for computing radiative transfer are the zonal and Monte Carlo methods [?]. However, these methods are not widely applied in comprehensive heat transfer calculations due to their large computational time and storage requirements. Also, the equations of radiative transfer are in non-differential form, a significant inconvenience when solved in conjunction with the differential equations of heat conduction, flow and combustion. Most of the current work on modelling energy transport in high-temperature media or chemically reacting flows uses Computational Fluid Dynamics (CFD) codes; see for instance [?, ?, ?]. Therefore, the models for solving the radiative transfer must be compatible with the numerical methods employed to solve the reacting flow equations. The zonal and Monte Carlo methods for solving radiative transfer problems are incompatible with the mathematical formulations used in CFD codes. The S_n discrete-ordinate methods [?]

appear to be reasonable compromises for solving the radiative transfer equations, but still one has to deal with large systems of algebraic equations, resulting from discretizing angular and spatial coordinates, that may be detrimental to the efficiency of the CFD code. For more details, the interested reader is referred to [?, ?].

In the field of glass manufacturing, the quality of the final product strongly depends on controlling the annealing process as molten glass is cooled down to room temperature. Recent developments in optical industries such as display technologies and lens manufacturing require glass objects having specific optical and physical properties. This has led to an increasing interest in accurate mathematical models which can predict the heat transfer involved in glass manufacturing, and hence to a better control over annealing process. Among these models, the Rosseland approximation [?] could be the most efficient, but fails to resolve accurately the boundary layers in the cooling processes. The simplified P_N approximations for RHT models is widely used in the literature. These approximations were first proposed in [?] and theoretically studied in [?]. In [?] the simplified P_N approximations were implemented for radiation in gas turbines, while in [?, ?] they were studied for the RHT in glass manufacturing. These simplified models are derived using an asymptotic analysis and they perform very well when the medium under consideration is isotropic and optically thick (opaque). In fact, in an opaque medium the system is close to a radiative equilibrium for which the assumptions of the simplified P_N equations are satisfied. A key advantage in simplified P_N approximations is the fact that the conduction-radiation equations are transformed to a mixed set of parabolic and elliptic equations independent of the angular directions, facilitating their numerical solution. Furthermore, comparisons presented in the previous references proved that in optically thick media (large absorption) the simplified P_N models approach the full radiative heat transfer problem with a lower computational cost and with greater accuracy than those obtained by the classical Rosseland approach traditionally used in many applications in glass manufacturing. In this paper, we adopt the simplified P_1 approximation to the conduction-radiation problem. We consider glass cooling models with eight frequency bands kindly provided by ITWM [?] and also analyzed in [?, ?] among others.

A key feature of the RHT in glass manufacturing problems is the existence of very high thermal gradients at the domain boundary at the start of the cooling process. One approach to capturing these steep gradients with numerical methods such as the conventional Finite Element Method (FEM) is to use a highly refined mesh close to the boundaries. However, the required refinement level, coupled with small time steps needed to capture the thermal radiation, may cause an extended solution time which can become prohibitive for industrial purposes. A more sophisticated approach arises from application of different variations of the partition of unity technique [?]; this involves enrichment of the finite element approximation space in order to become more efficient in dealing with high gradients. A relatively early work dealing with the enriched FEM for diffusion and convection problems can be found in [?] where the authors enriched the FEM with the analytical solution of the considered problem in one space dimension. Further enrichment approaches have since been applied to transient thermal effects. In [?] an enrichment approach was developed to deal with time-dependent geothermal problems. The transient nature of the solution was accounted for through optimizing the enrichment at each time step. In a further development a global-local enriched formulation for transient heat transfer, in which a linear interpolative basis is augmented by an exponential function of space or space and time, was presented in [?]. Time-dependent shape functions are used to handle the transient nature of the problem and these are supplemented by local analysis using various techniques in regions of high thermal gradient. Another enrichment strategy was developed in [?] where, instead of time-dependent enrichment, the transient nature of the problem is expressed in term of a combination of Gaussian functions that mimic the time evolution of the solution as well as its spatial variation. The main advantage of such a strategy is allowing the linear system built at the first time step to be retained, only updating the right hand side for each subsequent time step. The approach has recently been applied successfully for conduction-radiation in diffusive grey media [?] where a combination of hyperbolic and Gaussian functions were used to recover the solution. In this paper this approach is used to solve the RHT in glass. Unlike the previous work where the thermal radiation is restricted to grey media, glass may radiate heat over a wide spectrum of frequencies. The P_1 approximation requires dividing the continuous spectrum into several frequency bands, thus the thermal radiation must be evaluated at each band. An optimized

enrichment approach, to reduce the computational costs especially when a high number of intervals is needed, is discussed. Special attention is paid to solution within the boundary layers and at early time steps which are particularly important in the control of the glass annealing process. The performance of the proposed method is compared to the h -version FEM with a further validation using the full radiative transfer solution.

This paper is organized as follows. The governing equations for the RHT in glass cooling are stated in section 2. In section 3, we formulate the partition-of-unity finite element for the numerical solution of the coupled heat transfer equations. This section includes a semi-implicit scheme for the time integration and the finite element method for the space discretization. Numerical results are presented in section 6. Section 7 contains concluding remarks.

2 Equations for heat transfer in glass cooling

Let \mathcal{D} be a geometrical domain, with boundary $\partial\mathcal{D}$, of an absorbing and emitting glass material. We seek the temperature distribution $T(\mathbf{x}, t)$, where $\mathbf{x} \in \mathcal{D}$ and t is time, with a given initial temperature distribution

$$T(\mathbf{x}, 0) = T_0(\mathbf{x}), \quad \mathbf{x} \in \mathcal{D}. \quad (1)$$

The heat conduction in the medium \mathcal{D} is described by the energy equation

$$\rho c \frac{\partial T}{\partial t} - \nabla \cdot (\lambda \nabla T) = - \int_{\nu_1}^{\infty} \int_{S^2} \kappa(\nu) \left(B(T, \nu, n_{\text{glass}}) - I \right) d\Omega d\nu, \quad (\mathbf{x}, t) \in \mathcal{D} \times [0, \mathcal{T}), \quad (2)$$

where ρ denotes the density, c the specific heat capacity, ν the frequency, λ the thermal conductivity and κ the absorption coefficient. On the boundary the heat flux $\lambda \mathbf{n}(\hat{\mathbf{x}}) \cdot \nabla T$ is defined by heat convection and diffuse surface radiation

$$\lambda \mathbf{n}(\hat{\mathbf{x}}) \cdot \nabla T + h(T - T_b) = \epsilon \pi \int_0^{\nu_1} \left(B(T_b, \nu, n_b) - B(T, \nu, n_{\text{glass}}) \right) d\nu, \quad (\hat{\mathbf{x}}, t) \in \partial\mathcal{D} \times [0, \mathcal{T}), \quad (3)$$

where h is the convective heat transfer coefficient, T_b is a given ambient temperature of the surrounding, $\mathbf{n}(\hat{\mathbf{x}})$ denotes the outward normal at $\hat{\mathbf{x}}$ with respect to $\partial\mathcal{D}$, ϵ is the mean hemispheric surface emissivity in the opaque spectral region $\nu \in [0, \nu_1]$, where radiation is completely absorbed, and n_b and n_{glass} are the refractive indices of the surrounding medium and glass material, respectively. In the above equations, $B(T, \nu, n)$ is the spectral intensity of the black-body radiation given by the Planck function in a medium with refractive index n ,

$$B(T, \nu, n) = \frac{2\hbar\nu^3}{c_0^2} n^2 (e^{\hbar\nu/kT} - 1)^{-1}. \quad (4)$$

Here \hbar , k and c_0 are Planck's constant, Boltzmann's constant and the speed of radiation propagation in a vacuum, respectively [?].

The spectral intensity $I = I(\mathbf{x}, \Omega, \nu)$ at the space point \mathbf{x} , at the frequency ν and along the direction Ω , is obtained from the radiative transfer equation

$$\forall \nu > \nu_1 : \quad \Omega \cdot \nabla I + \kappa(\nu)I = \kappa(\nu)B(T, \nu, n_{\text{glass}}), \quad (\mathbf{x}, \Omega) \in \mathcal{D} \times S^2, \quad (5)$$

where S^2 denotes the unit sphere. At the boundary we consider a transmitting and specular reflecting condition

$$I(\hat{\mathbf{x}}, \Omega, \nu) = \varrho(\mathbf{n} \cdot \Omega)I(\hat{\mathbf{x}}, \Omega', \nu) + (1 - \varrho(\mathbf{n} \cdot \Omega))B(T_b, \nu, n_b), \quad (\hat{\mathbf{x}}, \Omega) \in \partial\mathcal{D}^- \times S^2, \quad (6)$$

where the boundary region $\partial\mathcal{D}^-$ is defined as

$$\partial\mathcal{D}^- = \left\{ \hat{\mathbf{x}} \in \partial\mathcal{D} : \mathbf{n}(\hat{\mathbf{x}}) \cdot \Omega < 0 \right\},$$

and Ω' is the specular reflection of Ω on $\partial\mathcal{D}$ given by

$$\Omega' = \Omega - 2(\mathbf{n} \cdot \Omega)\mathbf{n}.$$

In (6), $\varrho \in [0, 1]$ is the reflectivity obtained according to the Fresnel and Snell law. Thus, for an incident angle θ_1 given by $\cos \theta_1 = |\mathbf{n} \cdot \Omega|$ and Snell's law

$$n_b \sin \theta_2 = n_{\text{glass}} \sin \theta_1,$$

the reflectivity $\varrho(\mu)$, $\mu = |\mathbf{n} \cdot \Omega|$, is defined as follows

$$\varrho(\mu) = \begin{cases} \frac{1}{2} \left(\frac{\tan^2(\theta_1 - \theta_2)}{\tan^2(\theta_1 + \theta_2)} + \frac{\sin^2(\theta_1 - \theta_2)}{\sin^2(\theta_1 + \theta_2)} \right), & \text{if } |\sin \theta_1| \leq \frac{n_b}{n_{\text{glass}}}, \\ 1, & \text{otherwise.} \end{cases}$$

We assume that $n_{\text{glass}} > n_b$ and the hemispheric emissivity ϵ is related to the reflectivity ϱ by

$$\epsilon = 2n_{\text{glass}} \int_0^1 (1 - \varrho(\mu)) d\mu.$$

To minimize the number of parameters, the following non-dimensional variables are introduced

$$\mathbf{x}^* = \frac{\mathbf{x}}{\mathbf{x}_{\text{ref}}}, \quad \kappa^* = \frac{\kappa}{\kappa_{\text{ref}}}, \quad T^* = \frac{T}{T_{\text{ref}}}, \quad I^* = \frac{I}{I_{\text{ref}}},$$

where \mathbf{x}_{ref} , σ_{ref} , κ_{ref} , T_{ref} and I_{ref} are reference quantities. We also introduce

$$t^* = c\rho\kappa^*\mathbf{x}^{*2}\frac{T^*}{I^*} \quad \text{and} \quad \lambda^* = \frac{I^*}{\kappa^*T^*}.$$

With a diffusion scale, $\varepsilon \in (0, 1]$, defined as

$$\varepsilon = \frac{1}{\kappa^*\mathbf{x}^*},$$

we may write the radiative heat transfer (RHT) equations (1)-(6) in dimensionless form as

$$\begin{aligned} \varepsilon^2 \frac{\partial T}{\partial t} - \varepsilon^2 \nabla \cdot (\lambda \nabla T) &= - \int_{\nu_0}^{\infty} \kappa(\nu) \left(4\pi B(T, \nu, n_{\text{glass}}) - \int_{S^2} I(\mathbf{x}, \Omega, \nu) d\Omega \right) d\nu, \\ \forall \nu > \nu_1 : \quad \varepsilon \Omega \cdot \nabla I + \kappa(\nu) I &= \kappa(\nu) B(T, \nu, n_{\text{glass}}), \\ \varepsilon \lambda \mathbf{n}(\hat{\mathbf{x}}) \cdot \nabla T + h(T - T_b) &= \varepsilon \pi \int_0^{\nu_1} \left(B(T_b, \nu, n_b) - B(T, \nu, n_{\text{glass}}) \right) d\nu, \\ I(\hat{\mathbf{x}}, \Omega, \nu) &= \varrho(\mathbf{n} \cdot \Omega) I(\hat{\mathbf{x}}, \Omega', \nu) + (1 - \varrho(\mathbf{n} \cdot \Omega)) B(T_b, \nu, n_b), \\ T(\mathbf{x}, 0) &= T_0(\mathbf{x}), \end{aligned} \tag{7}$$

where we have dropped the * superscript for ease of notation. In this paper we assume that the spectral absorption coefficients $\kappa(\nu)$ are piecewise constant with respect to the frequency ν , *i.e.*,

$$\kappa(\nu) = \kappa_k, \quad \forall \nu \in [\nu_k, \nu_{k+1}), \quad k = 0, 1, \dots, N, \quad \nu_0 = 0, \tag{8}$$

with κ_k is constant and N is the total number of spectral bands. If we introduce the intensity of the k th spectral band

$$I^{(k)}(\mathbf{x}, \Omega) = \int_{\nu_k}^{\nu_{k+1}} I(\mathbf{x}, \Omega, \nu) d\nu,$$

then the RHT equations (7) transform to

$$\begin{aligned}
\varepsilon^2 \frac{\partial T}{\partial t} - \varepsilon^2 \nabla \cdot (\lambda \nabla T) &= - \sum_{k=1}^N \kappa_k \left(4\pi B^{(k)}(T, n_{\text{glass}}) - \varphi^{(k)} \right), \\
\varepsilon \Omega \cdot \nabla I^{(k)} + \kappa_k I^{(k)} &= \kappa_k B^{(k)}(T, n_{\text{glass}}), \\
\varepsilon \lambda \mathbf{n}(\hat{\mathbf{x}}) \cdot \nabla T + h(T - T_b) &= \varepsilon \pi \left(B^{(0)}(T_b, n_b) - B^{(0)}(T, n_{\text{glass}}) \right), \\
I^{(k)}(\hat{\mathbf{x}}, \Omega) &= \varrho(\mathbf{n} \cdot \Omega) I^{(k)}(\hat{\mathbf{x}}, \Omega') + (1 - \varrho(\mathbf{n} \cdot \Omega)) B^{(k)}(T_b, n_b), \\
T(\mathbf{x}, 0) &= T_0(\mathbf{x}),
\end{aligned} \tag{9}$$

where the mean intensity $\varphi^{(k)}$ and the Planck function $B^{(k)}$ are defined by

$$\varphi^{(k)}(\mathbf{x}) = \int_{S^2} I^{(k)}(\mathbf{x}, \Omega) d\Omega, \quad \text{and} \quad B^{(k)}(T, n) = \int_{\nu_k}^{\nu_{k+1}} B(T, \nu, n) d\nu.$$

The RHT equations (7) are widely accepted as an accurate model for radiation transport in participating and non-participating media. These equations do not have analytical solutions for arbitrary geometries and their numerical solution leads to computationally demanding problems due to the large set of dependent variables. For these reasons, numerous investigations are currently being carried out to derive approximate methods that are computationally less demanding than solving the equations (7). Among typical approximations to RHT we cite the Rosseland approach [?] and simplified P_N approximations [?, ?]. Indeed, a major reduction of the discrete phase space can be achieved, if one replaces the RHT equations by a new model which only involves physical quantities independent of the angular direction. One possibility to do so is the usage of the so-called simplified SP_N approximations. In this section we only set up the simplified SP_1 ; for further details we refer to [?, ?]. Thus, the SP_1 approximation for the radiative heat transfer equation reads

$$\begin{aligned}
\frac{\partial T}{\partial t} - \nabla \cdot (\lambda \nabla T) &= \sum_{k=1}^N \nabla \cdot \left(\frac{1}{3\kappa_k} \nabla \varphi^{(k)} \right), \\
-\nabla \cdot \left(\frac{\varepsilon^2}{3\kappa_k} \nabla \varphi^{(k)} \right) + \kappa_k \varphi^{(k)} &= 4\pi \kappa_k B^{(k)}(T, n_{\text{glass}}), \quad k = 1, \dots, N.
\end{aligned} \tag{10}$$

The boundary conditions are derived based on the asymptotic analysis in [?]. For the SP_1 approximation (10), $\varphi^{(k)}$ satisfies the boundary condition

$$\varphi^{(k)} + \left(\frac{1 + 3r_2}{1 - 2r_1} \frac{2\varepsilon}{3\kappa_k} \right) \mathbf{n}(\hat{\mathbf{x}}) \cdot \nabla \varphi^{(k)} = 4\pi B^{(k)}(T_b, n_b), \quad k = 1, \dots, N, \tag{11}$$

where the integrals r_1 and r_2 are defined by

$$r_1 = \int_0^1 \mu \rho(-\mu) d\mu, \quad r_2 = \int_0^1 \mu^2 \rho(-\mu) d\mu.$$

In summary, the SP_1 approximation of the RHT problem (9) can be reformulated as

$$\begin{aligned}
\frac{\partial T}{\partial t} - \nabla \cdot (\lambda \nabla T) &= \sum_{k=1}^N \nabla \cdot \left(\frac{1}{3\kappa_k} \nabla \varphi^{(k)} \right), & (\mathbf{x}, t) \in \mathcal{D} \times [0, \mathcal{T}), \\
-\nabla \cdot \left(\frac{\varepsilon^2}{3\kappa_k} \nabla \varphi^{(k)} \right) + \kappa_k \varphi^{(k)} &= 4\pi \kappa_k B^{(k)}(T, n_{\text{glass}}), & (\mathbf{x}, t) \in \mathcal{D} \times [0, \mathcal{T}), \\
\varepsilon \lambda \mathbf{n}(\hat{\mathbf{x}}) \cdot \nabla T + h(T - T_b) &= \varepsilon \pi \left(B^{(0)}(T_b, n_b) - B^{(0)}(T, n_{\text{glass}}) \right), & (\hat{\mathbf{x}}, t) \in \partial \mathcal{D} \times [0, \mathcal{T}), \\
\varphi^{(k)} + \left(\frac{1 + 3r_2}{1 - 2r_1} \frac{2\varepsilon}{3\kappa_k} \right) \mathbf{n}(\hat{\mathbf{x}}) \cdot \nabla \varphi^{(k)} &= 4\pi B^{(k)}(T_b, n_{\text{glass}}), & (\hat{\mathbf{x}}, t) \in \partial \mathcal{D} \times [0, \mathcal{T}), \\
T(\mathbf{x}, 0) &= T_0(\mathbf{x}), & \mathbf{x} \in \mathcal{D},
\end{aligned} \tag{12}$$

for $k = 1, 2, \dots, N$. It should be stressed that the enriched partition-of-unity finite element method proposed in the current study can also be extended to the simplified P₂ and the simplified P₃ from [?] without major conceptual modifications.

3 Time discretization approach

To integrate the equations (12) we divide the time interval $[0, \mathcal{T}]$ into equi-distributed subintervals $[t_n, t_{n+1}]$ with length $\Delta t = t_{n+1} - t_n$ for $n = 0, 1, \dots$. We use the notation w^n to denote the value of a generic function w at time t_n . Hence, applied to the system (12) a semi-implicit time stepping scheme results in

$$\begin{aligned}
\frac{T_{n+1} - T_n}{\Delta t} - \nabla \cdot (\lambda \nabla T_{n+1}) &= \sum_{k=1}^N \nabla \cdot \left(\frac{1}{3\kappa_k} \nabla \varphi^{(k)} \right), \\
-\nabla \cdot \left(\frac{\varepsilon^2}{3\kappa_k} \nabla \varphi^{(k)} \right) + \kappa_k \varphi^{(k)} &= 4\pi \kappa_k B^{(k)}(T_n, n_{\text{glass}}), \\
\varepsilon \lambda_c \mathbf{n}(\hat{\mathbf{x}}) \cdot \nabla T_{n+1} + h(T_{n+1} - T_b) &= \varepsilon \pi \left(B^{(0)}(T_b, n_b) - B^{(0)}(T_n, n_{\text{glass}}) \right), \\
\varphi^{(k)} + \left(\frac{1 + 3r_2}{1 - 2r_1} \frac{2\varepsilon}{3\kappa_k} \right) \mathbf{n}(\hat{\mathbf{x}}) \cdot \nabla \varphi^{(k)} &= 4\pi B^{(k)}(T_b, n_{\text{glass}}), \quad k = 1, \dots, N, \\
T^0(\mathbf{x}) &= T_0(\mathbf{x}).
\end{aligned} \tag{13}$$

Notice that the mean radiative intensity φ does not depend explicitly on the time variable, however its dynamics depends on the time evolution of the medium temperature. Thus, one could replace the mean radiative intensity φ in (13) by φ^{n+1} to emphasis its implicit dependence on the time. The procedure to advance the solution from the time t_n to the next time t_{n+1} can be carried out in the following two steps:

Step 1. Radiation stage: Solve for $\varphi_{n+1}^{(k)}$

$$\begin{aligned}
-\nabla \cdot \left(\frac{\varepsilon^2}{3\kappa_k} \nabla \varphi_{n+1}^{(k)} \right) + \kappa_k \varphi_{n+1}^{(k)} &= 4\pi \kappa_k B^{(k)}(T_n, n_{\text{glass}}), \\
\varphi_{n+1}^{(k)} + \left(\frac{1 + 3r_2}{1 - 2r_1} \frac{2\varepsilon}{3\kappa_k} \right) \mathbf{n}(\hat{\mathbf{x}}) \cdot \nabla \varphi_{n+1}^{(k)} &= 4\pi B^{(k)}(T_b, n_{\text{glass}}), \quad k = 1, \dots, N.
\end{aligned} \tag{14}$$

Step 2. Conduction stage: Solve for T_{n+1}

$$\begin{aligned}
\frac{T_{n+1} - T_n}{\Delta t} - \nabla \cdot (\lambda \nabla T_{n+1}) &= \sum_{k=1}^N \nabla \cdot \left(\frac{1}{3\kappa_k} \nabla \varphi_{n+1}^{(k)} \right), \\
\varepsilon \lambda_c \mathbf{n}(\hat{\mathbf{x}}) \cdot \nabla T_{n+1} + h(T_{n+1} - T_b) &= \varepsilon \pi \left(B^{(0)}(T_b, n_b) - B^{(0)}(T_n, n_{\text{glass}}) \right), \\
T^0(\mathbf{x}) &= T_0(\mathbf{x}).
\end{aligned} \tag{15}$$

For simplicity in presentation we rewrite the equations (14) and (15) in a compact form as

$$U - \nabla \cdot (A \nabla U) = F, \tag{16a}$$

$$\alpha U + \mathbf{n}(\hat{\mathbf{x}}) \cdot \nabla U = f, \tag{16b}$$

where, for the mean radiative intensity $U = \varphi^{n+1}$

$$A = \frac{\varepsilon^2}{3\kappa(\sigma + \kappa)}, \quad F = 4\pi B(T_n), \quad \alpha = \frac{3(\sigma + \kappa)}{2\varepsilon}, \quad f = \frac{6(\sigma + \kappa)}{\varepsilon} \pi B(T_b).$$

For the temperature field $U = T_{n+1}$

$$A = \lambda \Delta t, \quad F = T_n + \nabla \cdot \left(\frac{\Delta t}{3(\sigma + \kappa)} \nabla \varphi^{n+1} \right), \quad \alpha = \frac{\hbar}{\varepsilon \lambda}, \quad f = \frac{\hbar}{\varepsilon \lambda} T_b.$$

Note that the above time integration scheme is only first-order accurate and conditionally stable. Other high-order semi-implicit methods can also be applied. In the solution procedure, only linear systems have to be solved at each time step to update the temperature and the mean radiative intensity. We should also point out that the source term in (14) contains the explicit temperature variable T^n . It is possible to treat this term implicitly by solving first the conduction stage followed by the radiation stage. In the considered test examples, both treatments produce the same results. Another way to solve the above equations is to involve all the stages implicitly in time and solve one single equation of the form (16) for $U = (T_{n+1}, \varphi^{n+1})^T$. This procedure leads to a coupled nonlinear system to be solved at each time step. However, the numerical solution of such nonlinear system is computationally demanding and it may limit the efficiency of the algorithm.

4 Variational formulation

Since the spatial discretization approach is based on the finite element method, a variational formulation of the problem is established for the problem (16). The following Sobolev space is introduced

$$V = \{v \in H^1(\Omega); v = 0 \text{ on } \partial\Omega\}, \quad (17)$$

where $H^1(\Omega)$ denotes the set of square integrable functions whose first derivatives are also square integrable. The weak variational formulation of the problem can be described as: Find $u \in V$ such that

$$\mathbf{a}(u, v) = \mathbf{b}(v), \quad \forall v \in V, \quad (18)$$

where v is a test function in V and \mathbf{a}, \mathbf{b} are bilinear and linear forms defined respectively, as

$$\mathbf{a}(u, v) = \int_{\Omega} v u d\mathbf{x} - \int_{\Omega} A v \nabla^2 u d\mathbf{x}. \quad (19)$$

$$\mathbf{b}(v) = \int_{\Omega} v F d\mathbf{x}. \quad (20)$$

Using the divergence theorem gives

$$\int_{\Omega} v \nabla^2 u d\mathbf{x} = \oint_{\partial\Omega} v \nabla u \cdot \mathbf{n} d\mathbf{x} - \int_{\Omega} \nabla v \cdot \nabla u d\mathbf{x}. \quad (21)$$

Substituting (21) into the bilinear form results in

$$\mathbf{a}(u, v) = \int_{\Omega} v u d\mathbf{x} - \oint_{\partial\Omega} A v \nabla u \cdot \mathbf{n} d\mathbf{x} + \int_{\Omega} A \nabla v \cdot \nabla u d\mathbf{x}, \quad (22)$$

which could be simplified into

$$\mathbf{a}(u, v) = \int_{\Omega} (A \nabla v \cdot \nabla u + v u) d\mathbf{x} - \oint_{\partial\Omega} A v \nabla A \cdot \mathbf{n} d\mathbf{x}. \quad (23)$$

After substitution of the boundary condition (16b) into (23) the bilinear form reads

$$\mathbf{a}(u, v) = \int_{\Omega} (A \nabla v \cdot \nabla u + v u) d\mathbf{x} + \oint_{\partial\Omega} A v (\alpha u - f) d\mathbf{x}. \quad (24)$$

Let the domain Ω be partitioned into N_e non-overlapping sub-domains $\Omega^n, n = 1, \dots, N_e$. Each sub-domain, or finite element in the engineering terminology, is given through a coordinate transformation $\mathbf{r} = L^k(\boldsymbol{\eta})$

between the real space and the local system $\boldsymbol{\eta} = (\eta_1, \eta_2) \in \mathcal{L}$. The used elements are of triangular type with $\mathcal{L} = \mathcal{T} \times [-1, 1]$ where \mathcal{T} stands for the triangular domain

$$\mathcal{T} = \{ \eta_1 \geq 0, \eta_2 \geq 0, \eta_1 + \eta_2 \leq 1 \}. \quad (25)$$

Using a conventional piecewise linear finite element space, the quantity u on Ω^n is approximated as

$$u \simeq u_h^n = \sum_{p=1}^{\#\text{vert}} \mathcal{N}_p(\boldsymbol{\eta}) u_p^n, \quad (26)$$

where \mathcal{N}_p stands for the (P_1) Lagrangian polynomial on \mathcal{L} and u_p are the nodal values corresponding to the vertices of \mathcal{L} with $\#\text{vert} = 3$ for the triangular type elements used here. The linear approximation (26) requires the mesh size to be small enough to capture the variable field. This limitation is to be alleviated if a set of local enrichment functions are included (ref. `ijne`, `jca`).

5 Approximation by field-enriched finite elements

Next, we formulate the finite element solution to U as

$$U \simeq u_h^n(\mathbf{x}) = \sum_{j=1}^{N_d} u_j^n \mathcal{N}_j(\mathbf{x}), \quad (27)$$

where N_d is the number of solution mesh points in the partition Ω_h . The functions u_j^n are the corresponding nodal values of $u_h^n(\mathbf{x})$. They are defined as $u_j^n = u_h^n(\mathbf{x}_j)$ where $\{\mathbf{x}_j\}_{j=1}^{N_d}$ are the set of solution mesh points in the partition \mathcal{D}_h . In (27), $\{\mathcal{N}_j\}_{j=1}^{N_d}$ are the set of global nodal basis functions of V_h characterized by the property $\mathcal{N}_i(\mathbf{x}_j) = \delta_{ij}$ with δ_{ij} denoting the Kronecker symbol. We introduce $\{\mathbf{x}_1, \dots, \mathbf{x}_M\}$ as the set of M nodal points in the element \mathcal{K}_j . Hereafter, unless otherwise stated, the subscripts h and j are used to refer to coefficients associated with the whole mesh \mathcal{D}_h and a mesh element \mathcal{K}_j , respectively. The approximation space is then defined as

$$\tilde{V}_h^0 = \text{span} \left\{ \mathcal{N}_h, \quad u_h = \sum_{j=0}^M u_j \mathcal{N}_j \right\}.$$

Using the partition of unity method [?] it is possible to enrich the solution space with basis functions that have better approximation properties than the conventional polynomial basis functions. To enrich the solution space here we propose a hyperbolic tangent function, which is selected because of its ability to model a locally high gradient in an otherwise uniform field. This enrichment may be applied to an edge, e , forming part of $\partial\mathcal{D}$. For example, if an edge lies at the position $x = x_e$ such that the domain \mathcal{D} lies in $x > x_e$, we define a family of enrichment functions

$$\bar{G}_{le}^{tanh} = \frac{V_1 + V_2}{2} + \frac{V_1 - V_2}{2} \tanh\left(\frac{x - x_e}{h_l}\right), \quad l = 1, 2, \dots, L, \quad (28)$$

where V_1 , V_2 and h_l are the control parameters of the functions \bar{G}_{le}^{tanh} . Such families of functions may be written for all appropriate edges comprising $\partial\mathcal{D}$. The global derivatives are then given by

$$\begin{aligned} \frac{\partial \bar{G}_{le}^{tanh}}{\partial x} &= \frac{(V_1 - V_2)}{2h_l} \left(1 - \tanh^2\left(\frac{x - x_e}{h_l}\right) \right), \\ \frac{\partial \bar{G}_{le}^{tanh}}{\partial y} &= 0. \end{aligned}$$

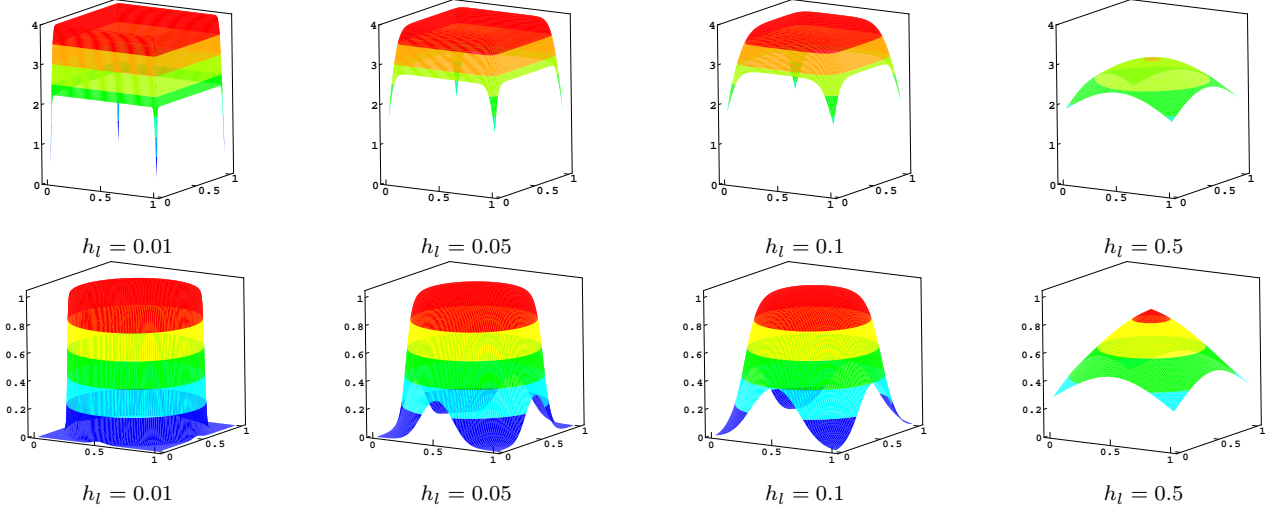


Figure 1: Illustration for different orders of enrichment functions of the Gaussian (first row) and the hyperbolic tangent on four edges of a square (second row) and on a circle (third row).

Another variation of this function considered here is for a circular edge $r = r_e$ where polar coordinates are used

$$\bar{G}_{le}^{tanh} = \frac{V_1 + V_2}{2} + \frac{V_1 - V_2}{2} \tanh\left(\frac{r - r_e}{h_l}\right), \quad l = 1, 2, \dots, L, \quad (29)$$

with r being the radial coordinate. Then the global derivatives are given by

$$\begin{aligned} \frac{\partial \bar{G}_{le}^{tanh}}{\partial x} &= \frac{x(V_1 - V_2)}{2rh_l} \left(1 - \tanh^2\left(\frac{r - r_e}{h_l}\right)\right), \\ \frac{\partial \bar{G}_{le}^{tanh}}{\partial y} &= \frac{y(V_1 - V_2)}{2rh_l} \left(1 - \tanh^2\left(\frac{r - r_e}{h_l}\right)\right). \end{aligned}$$

In the present work, we consider hyperbolic tangent enrichment as the summation of functions \bar{G} over all edges at which boundary layers may develop, *i.e.* the family of these enrichment functions to be injected into the analysis is

$$G_l^{tanh} = \sum_{e=1}^{NE} \bar{G}_{le}^{tanh}, \quad l = 1, 2, \dots, L \quad (30)$$

where NE is the number of edges over which this enrichment is applied. Note that the Gaussian enrichment is used to approximate the diffusion effect inside the physical domain, whereas the hyperbolic tangent enrichment is used to approximate a sharp gradient across the boundary layer at the edges. To illustrate the different types of enrichment we display them in Figure 1. The two variations of G_l^{tanh} are shown, with the first variation being taken as the sum over the four edges of a square domain.

If a combination of the two types of enrichment is to be used, the nodal values as in (27) can be rewritten at any time $t = t_n$ as

$$u_j^n = \sum_{q=1}^Q A_j^{q,n} G_q^{gauss} + \sum_{l=1}^L B_j^{l,n} G_l^{tanh}. \quad (31)$$

The finite element method is now used to find the values of the new set of unknowns $A_j^{q,n}$ and $B_j^{l,n}$ instead

Table 1: Absorption coefficients for the eight frequency bands used in our simulations.

| band i | $\nu_{i-1} [10^{13} s^{-1}]$ | $\nu_i [10^{13} s^{-1}]$ | $\lambda_i [\mu m]$ | $\lambda_{i-1} [\mu m]$ | $\kappa_i [m^{-1}]$ |
|----------|------------------------------|--------------------------|---------------------|-------------------------|---------------------|
| - | 0 | 2.9334638 | 7.00 | ∞ | opaque |
| 1 | 2.9334638 | 3.4223744 | 6.0 | 7.0 | 7136.00 |
| 2 | 3.4223744 | 3.7334994 | 5.5 | 6.0 | 576.32 |
| 3 | 3.7334994 | 4.5631659 | 4.5 | 5.5 | 276.98 |
| 4 | 4.5631659 | 5.1335616 | 4.0 | 4.5 | 27.98 |
| 5 | 5.1335616 | 5.8669276 | 3.5 | 4.0 | 15.45 |
| 6 | 5.8669276 | 6.8447489 | 3.0 | 3.5 | 7.70 |
| 7 | 6.8447488 | 102.6712329 | 0.2 | 3.0 | 0.50 |
| 8 | 102.6712329 | ∞ | 0.0 | 0.2 | 0.40 |

of the nodal values u_j^n as before. Using the nodal values (31) to rewrite (27) we obtain

$$u^n = \sum_{j=1}^M \sum_{q=1}^Q A_j^{q,n} \mathcal{N}_j G_q^{gauss} + \sum_{j=1}^M \sum_{l=1}^L B_j^{l,n} \mathcal{N}_j G_l^{tanh}. \quad (32)$$

Thus, the new approximation space becomes

$$\tilde{V}_h^1 = \text{span} \left\{ L_h, \quad u_h = \sum_{j=1}^M \sum_{q=1}^Q A_j^q \mathcal{N}_j G_q^{gauss} + \sum_{j=1}^M \sum_{l=1}^L B_j^l \mathcal{N}_j G_l^{tanh} \right\}.$$

It is worth remarking that the proposed enrichment functions are written in terms of the global coordinates \mathbf{x} , but they are multiplied by the nodal shape functions \mathcal{N}_j . In this sense the additional enrichment takes on a local character. It is evident that the enrichment proposed here for the transient conduction-radiation problems is time independent. This is possible because the combination of enrichments is chosen so that the temporal nature of the solution is approximated as well as the spatial behavior. Different authors have used time-dependent enrichment in solving diffusion problems (see for example [?, ?]). A major advantage of the time independent enrichments when considered with a finite element formulation similar to the one presented here is the ability to retain the system matrix assembled at the first time step to be reused at later time steps without alteration. Since only the right-hand side of the linear system of equations changes at subsequent time steps, one may factorize the matrix using an LU decomposition at the first time step thus the solution is reduced to successive backward/forward substitutions. This can significantly increase the efficiency when a large number of time steps is needed, compared to updating the matrix and fully solving the system at every time step.

6 Numerical results and applications

In this section we present numerical results for two test examples taken from the glass cooling process. The focus is on examining the numerical performance of the PUFEM algorithm described above and comparing its efficiency to the standard FEM. In the first example, the PUFEM solution is also compared to the solution obtained using the full radiative heat transfer model. In both examples, the enrichment is applied

Table 2: Reference parameters considered in the present work for glass cooling process.

| | |
|---------------------------|---|
| Density | $\rho_\infty = 2514.8 \text{ kg/m}^3$ |
| Specific heat capacity | $c_p = 1239.6 \text{ J/kgK}$ |
| Speed of light in vacuum | $c = 2.9979 \times 10^8 \text{ m/s}$ |
| Plank constant | $h_P = 6.62608 \times 10^{-34} \text{ Js}$ |
| Boltzmann constant | $k_B = 1.38066 \times 10^{-23} \text{ J/K}$ |
| Thermal conductivity | $\alpha = 1.672 \text{ Wm/K}$ |
| Convective heat transfer | $\xi = 0.001$ |
| Hemispheric emissivity | $\epsilon = 0.92$ |
| Refractive index of air | $n_a = 1$ |
| Refractive index of glass | $n_g = 1.46$ |
| Initial temperature | $T_0 = 1000 \text{ K}$ |
| Ambient temperature | $T_b = 300 \text{ K}$ |

on elements of the same order as in the finite elements the method being compared against, that is linear elements for the first example and quadratic elements for the second example. The presented results for cooling of a glass plate in the first example and a glass disc in the second, can be typical fabrication steps in glass manufacturing. The non-opaque frequency interval (ν_0, ∞) is approximated by an eight-band model studied in [?, ?]. Since the data are originally defined by wavelength intervals $[\lambda_{i-1}, \lambda_i]$, we computed the corresponding frequency bands using the relation

$$\nu_i = \frac{c_0}{\lambda_i n_{glass}}.$$

The eight wavelength bands and their associated absorption coefficients are listed in Table 1. It is evident from this table that the material is non-grey and the optical properties strongly change with the wavelength. In addition, the glass is considered to be opaque to radiation for wavelengths larger than a cut-off wavelength equal to $7 \mu\text{m}$. In all the computations reported herein, we used data listed in Table 2. In this study we highlight the effect of an instantaneous change in the ambient temperature from 1000 K to 300 K , causing a sharp drop in temperature across a boundary layer that can be very thin depending on the physical properties of the enclosure. As a thinner layer is considered the problem becomes more challenging to solve with the conventional FEM. To take this effect into consideration in the first example, two values of the diffusion scale $\varepsilon = 1$ and $\varepsilon = 0.5$ are considered, which correspond to two different optical regimes.

In the current study, to evaluate elementary matrix entries all the integrals are evaluated numerically using standard Gaussian quadrature. The number of integration points is chosen such that the results are not affected by the integration errors. It should be stressed that for the test examples considered in this paper, the total number of integration points used in the PUFEM is smaller than in the corresponding FEM model. The resulting linear systems of algebraic equations are solved using a direct solver.

6.1 Glass cooling in a plate enclosure

As a first test example we consider a unit glass square. Two different optical regimes are considered, corresponding to two different values of the non-dimensional parameter ε . Since the SP_N approximations were derived asymptotically for $\varepsilon \ll 1$ the results should better agree with the full RHT solution when ε is smaller (optically thick regime). The aim here is to conduct a comparative study of the performance of the proposed PUFEM to that of the conventional h -adaptive FEM with the latter being the usual approach used in glass manufacturing. To this end we consider four FEM meshes, the statistics of which are summarized

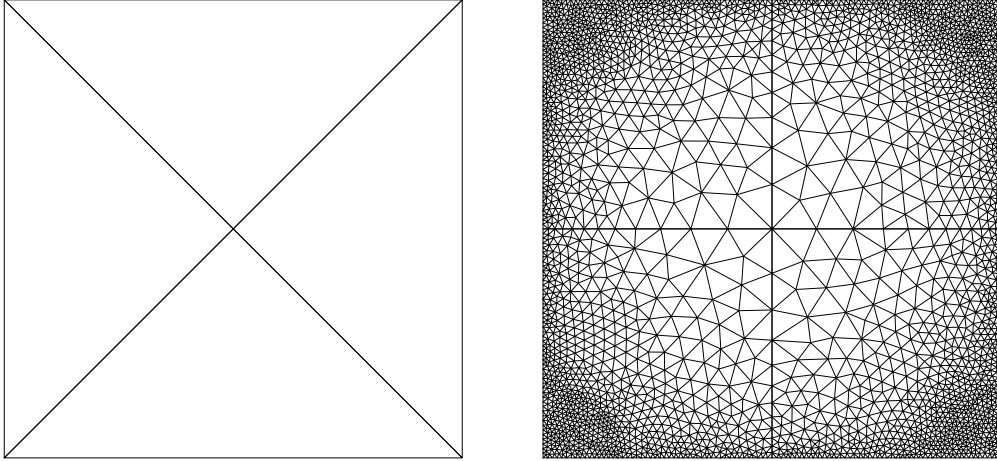


Figure 2: Comparison between the PUFEM mesh (left) and the coarse FEM mesh (right) for the glass cooling in a plate enclosure.

Table 3: Mesh statistics for the meshes used in the FEM.

| | Mesh A | Mesh B | Mesh C | Mesh D |
|---------------|--------|--------|--------|--------|
| # of elements | 2947 | 11389 | 44761 | 177457 |
| # of nodes | 5496 | 21984 | 87936 | 351744 |

in Table 3. For the PUFEM we use a mesh with five nodes and four elements as shown in the left plot in Figure 2. Linear three-noded elements are used in both the FEM and the PUFEM, the latter also being enriched using five hyperbolic functions (*i.e.* $Q = 5$). In this example, the same mesh as well as the same enrichment for the PUFEM are retained for solving the eight radiative mean intensities $\varphi^{(k)}$ ($k = 1, 2, \dots, 8$) and the temperature T . For comparison purpose, the PUFEM mesh is shown along side the coarse FEM mesh (Mesh A) in Figure 2. It is obvious that the total number of degrees of freedom in the PUFEM is just a small fraction of that with the coarse FEM mesh. In order to assess the accuracy of the considered PUFEM and FEM with respect to the time integration scheme we run the simulations using three different time steps namely, $\Delta t = 10^{-6}$, 10^{-7} and 10^{-8} . It should be noted that the five enrichment functions used in this example are based on the behaviour of the solution. In this type of problem the gradient can vary from infinity, at the start of the cooling, to zero at the steady state. Thus the first enrichment function is chosen to be of the highest gradient allowed by the machine precision. The fifth enrichment function is chosen to be of a gradient close to zero. The functions from two to four are designed such that each function is of a gradient smaller than its preceding and larger than its succeeding. Note that the difference in the gradient between any pair of successive enrichments is limited by two factors. First the difference should be small enough to enable smooth recovery of the entire time history. In other words it is possible to approximate the solution gradient at any simulation time using one of, or a combination of, these functions. The second limitation is related to the numerical stability because, if the difference between two successive enrichment functions and the next is too small to be observed by the given accuracy (double precision here), the two successive enrichment functions become indistinguishable from the numerical point of view. Hence, the linear system resulting from such enrichment is highly ill-conditioned or even singular. More details about the choice of the enrichment functions can be found in [?, ?].

We first evaluate the accuracy of the PUFEM and the FEM for resolving the boundary layers for the cooling case with the optical scale $\varepsilon = 0.5$. In Figure 3 we present the temperature variation along the domain edge ($y = 0$) at different simulation times using the considered meshes. Similar plots for the cooling

case but with $\varepsilon = 1$ are displayed in Figure 4. In each plot in these figures, the temperature at the domain edge is depicted for the three considered timestep sizes. Note that for a given simulation time the number of time steps for $\Delta t = 10^{-6}$ is 10 times and 100 times the number of time steps for $\Delta t = 10^{-7}$ and for $\Delta t = 10^{-8}$, respectively. It is evident in both figures that the FEM solution at early simulation times and with coarser meshes, exhibits strong oscillations that are reduced by refining the mesh. Independently of the mesh refinement, these oscillations damp out at later simulation times. An interesting observation is that the pattern of these oscillations seems to be unaffected by the timestep size or the diffusion scale ε . For instance, the boundary pattern found in Mesh A seems similar to the one found in Mesh B but with different amplitudes. Even for the fine meshes Mesh C and Mesh D at the simulation time $t = 2 \times 10^{-6}$, T seems to have small-amplitude counterparts to the major spikes found in the results obtained for the coarse Mesh A. This may be attributed to the fact that each of these meshes is a subset of another through its refinement. In comparison with the PUFEM solutions, it is clear that these spurious boundary oscillations are completely absent in the results obtained using the PUFEM. It is also clear from the results presented in Figure 3 and Figure 4 that the simulations with the time step $\Delta t = 10^{-7}$ overlap those obtained using $\Delta t = 10^{-8}$ for all simulation times. A small discrepancy between the results obtained using $\Delta t = 10^{-6}$ and other time steps can also be detected at early simulation times. The FEM solution on coarse meshes seems to be less sensitive to the selection of the time step Δt . This is to be expected as the space discretization error dominates the global error whereas on finer meshes the time discretization becomes more dominant. Similarly, the PUFEM solution shows sensitivity to the selection of the time step like the FEM solution on finer meshes. As the simulation time increases, this sensitivity with respect to Δt in both methods becomes negligible. However, the PUFEM still shows sensitivity at the time $t = 4 \times 10^{-6}$ for $\varepsilon = 0.5$ and at time $t = 8 \times 10^{-6}$ for $\varepsilon = 1$, unlike the FEM on the fine mesh Mesh D, which seems to be less sensitive at the respective time. Bearing in mind the slight change in the results using $\Delta t = 10^{-7}$ and using $\Delta t = 10^{-8}$ at the expense of rather significant increase in CPU times, the time step $\Delta t = 10^{-7}$ is believed to be adequate to obtain numerical results free of time integration effects. Hence, the results presented hereafter are based on using $\Delta t = 10^{-7}$.

To further investigate the effect of FEM meshes on the resolution of boundary layers, Figure 5 illustrates the temperature variation along the domain edge ($y = 0$) at different simulation times obtained for $\varepsilon = 0.5$ where the four considered FEM meshes and the PUFEM are included in the same plots for a better insight. The corresponding results obtained for $\varepsilon = 1$ are shown in Figure 6. Note that the selected simulation times are considered in order to compare the temperature features on the domain edge obtained using FEM on different meshes to those obtained using the PUFEM on the very coarse mesh shown in Figure 2 by keeping the time step fixed to $\Delta t = 10^{-7}$. As in the previous simulations, the oscillations on coarse FEM meshes are noted where the correspondence between spikes of different meshes can be easily recognized. The plots at early instants consistently show the average edge temperature as predicted by coarse FEM meshes is higher than that predicted by fine FEM meshes with the finite element solution in general converging towards the solution on the fine Mesh D as the simulation time progresses. The oscillations in the temperature results obtained using the FEM on Mesh C are damped out first, then followed by Mesh B and at later times by Mesh A as all the three converge toward the results obtained using the FEM on Mesh D. In comparison, the PUFEM results seem to start at a higher temperature before converging towards the FEM on Mesh D in a similar fashion to the coarse finite element meshes. However, some oscillations in time evolution are observed here, where the PUFEM starts higher then becomes lower before becoming close to those obtained using FEM on Mesh D; finally it seems slightly at a lower temperature than FEM on Mesh D. As the solution evolves in time, a significant difference in temperature at the domain corners is observed between the FEM and the PUFEM.

Our next concern with this example is to compare the results obtained using the PUFEM for the simplified P_1 model (12) to those from a direct solver for the full radiative heat transfer equations (7). To this end we solve the RHT equations (7) using the well-established Diffusion Synthetic Acceleration (DSA) method. The DSA method uses the diffusion approach to accelerate the source iteration which has been widely used in computational radiative transfer. We refer to [?, ?] for the implementation of the method and further discussions on other direct methods can be found therein. The S_8 discrete-ordinate

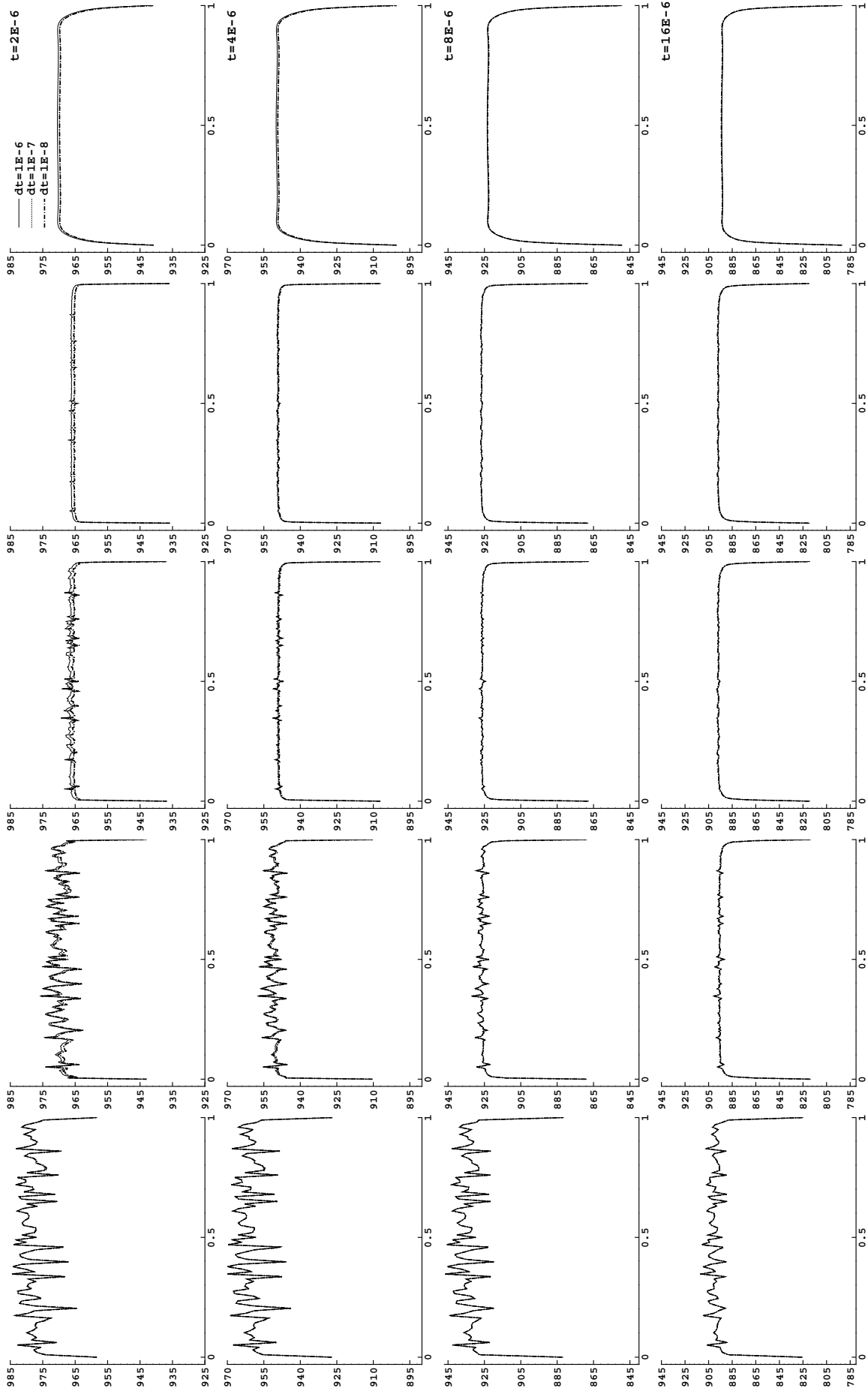


Figure 3: Comparison of the temperature along the domain edge ($y = 0$) using different timesteps for the PUFEM and the FEM on different meshes at time $t = 2 \times 10^{-6}$ (first row), 4×10^{-6} (second row), 8×10^{-6} (third row) and 16×10^{-6} (fourth row) for $\varepsilon = 0.5$. Here the results are shown for FEM on Mesh A (first column), FEM on Mesh B (second column), FEM on Mesh C (third column), FEM on Mesh D (fourth column) and PUFEM (fifth column).

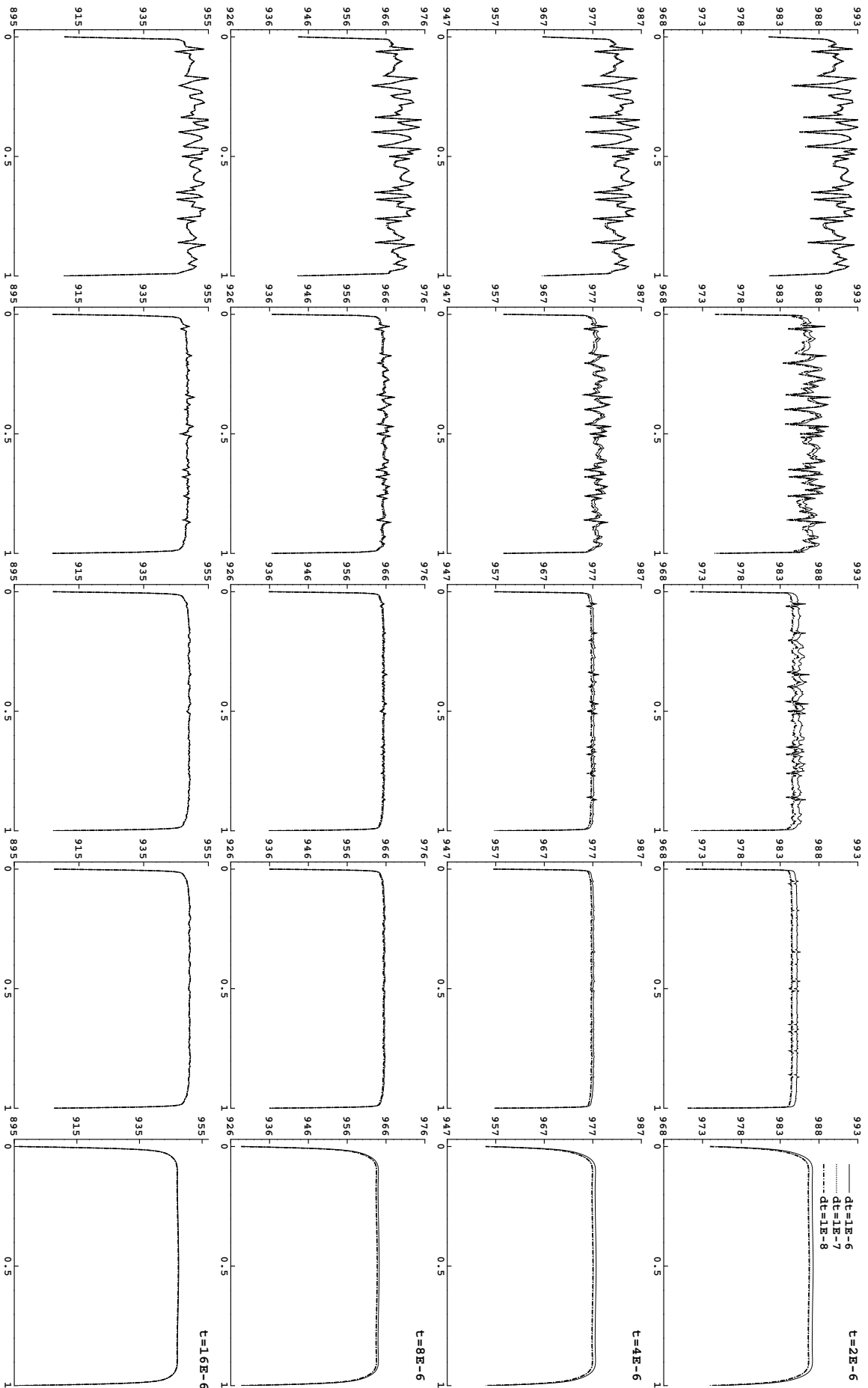


Figure 4: The same as Figure 3 but for $\epsilon = 1$

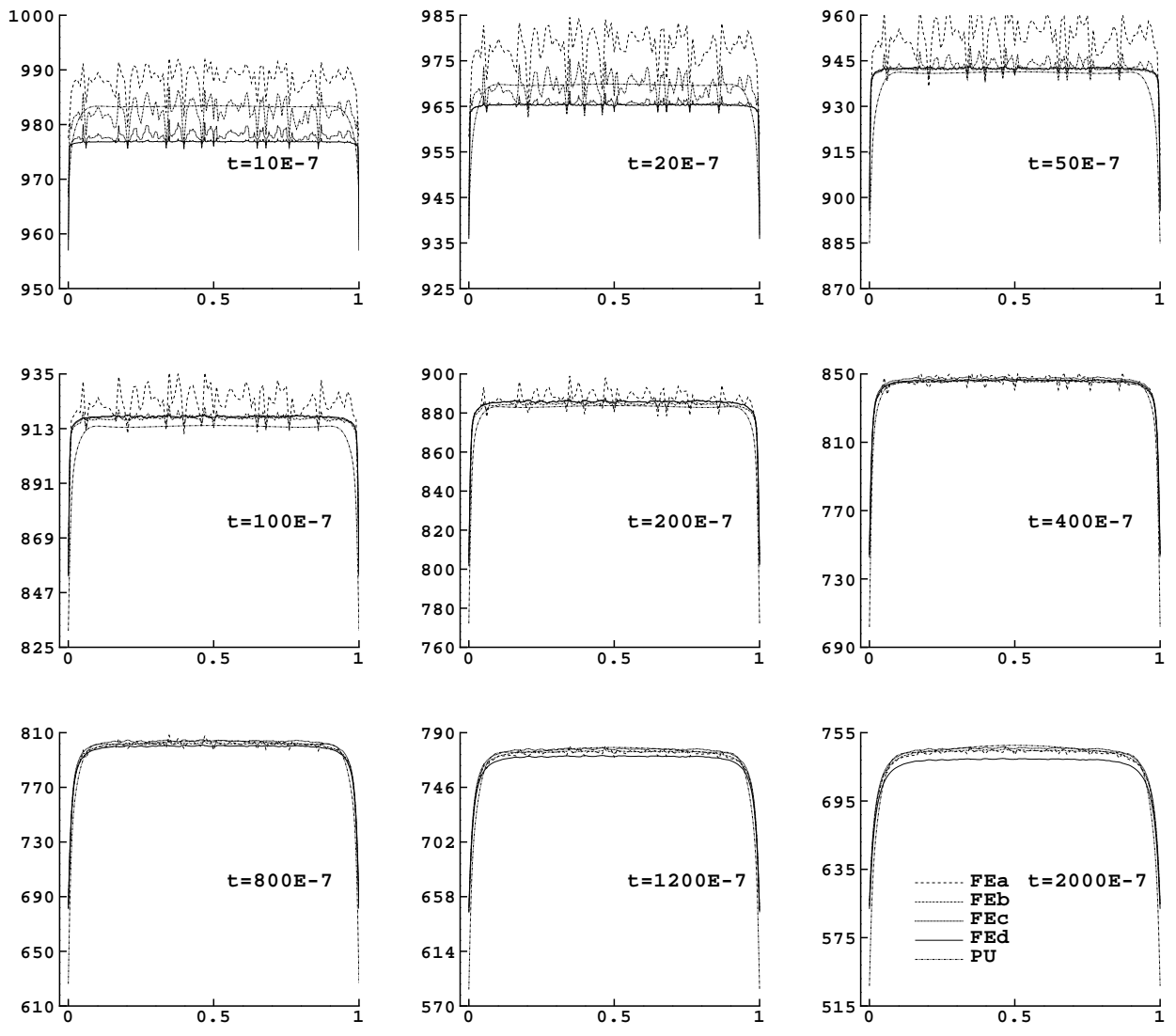


Figure 5: Comparison of the temperature along the domain edge ($y = 0$) using FEM and PUFEM at different instants using $\varepsilon = 0.5$.

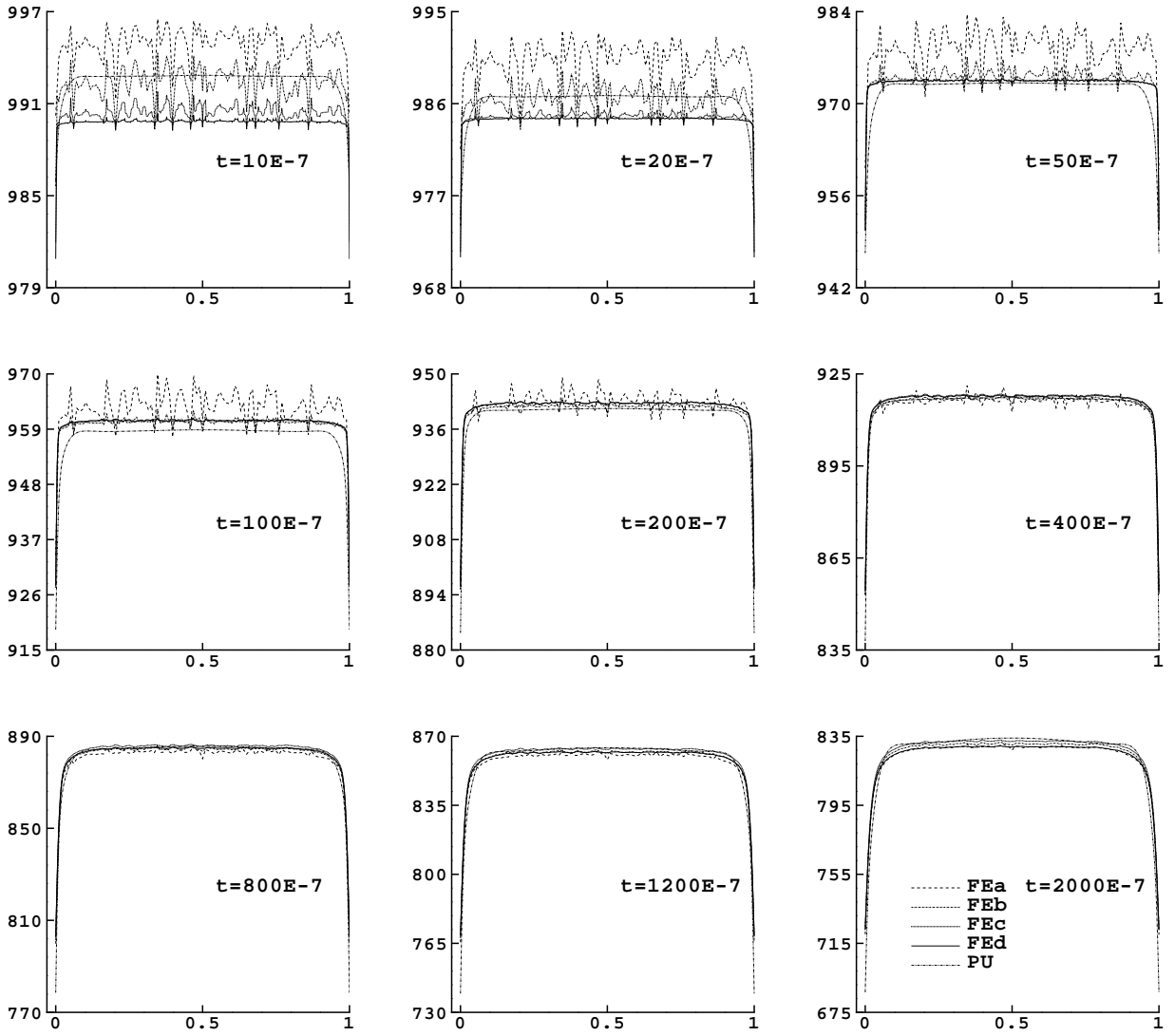


Figure 6: The same as Figure 5 but for $\varepsilon = 1$.

algorithm is selected for the discretization of the angle variable and a mesh of 100×100 grid-points is used in our computations, yielding a linear system with 64×10^5 unknowns which has to be solved for each time step. Here, we also consider the canonical Rosseland approach widely used in computational radiative heat transfer. This approach consists of replacing the RHT equations (9) by the following diffusion problem

$$\begin{aligned}
\frac{\partial T}{\partial t} - \nabla \cdot ((\lambda + \lambda_R) \nabla T) &= 0, & (\mathbf{x}, t) \in \mathcal{D} \times (0, \mathcal{T}], \\
\varepsilon \lambda \mathbf{n}(\hat{\mathbf{x}}) \cdot \nabla T + \hbar T &= \hbar T_b, & (\hat{\mathbf{x}}, t) \in \partial \mathcal{D} \times (0, \mathcal{T}], \\
T(\mathbf{x}, 0) &= T_0(\mathbf{x}), & \mathbf{x} \in \mathcal{D},
\end{aligned} \tag{33}$$

where

$$\lambda_R = \frac{16\pi}{3(\sigma + \kappa)} a_R T^3.$$

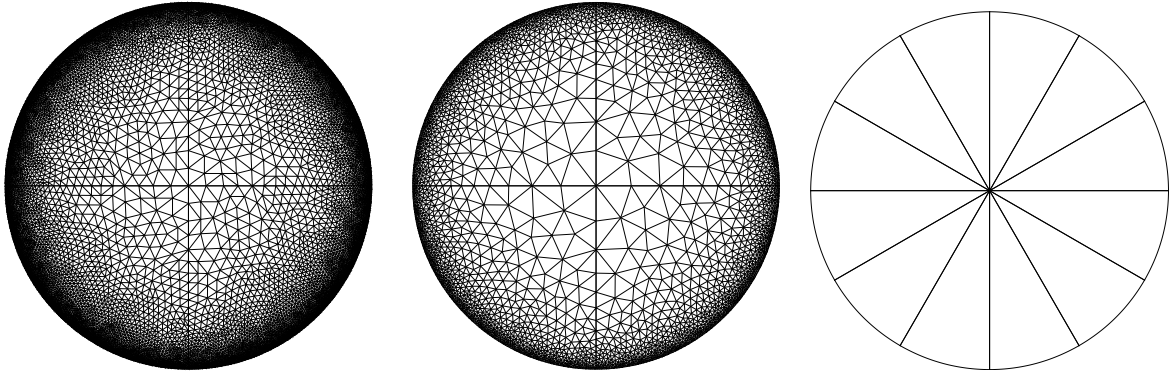


Figure 7: Comparison of the considered meshes (from left to right): FEMf (62785 nodes, 30608 elements), FEMc (16089 nodes, 7652 elements) and PUFEM (37 nodes, 12 elements)

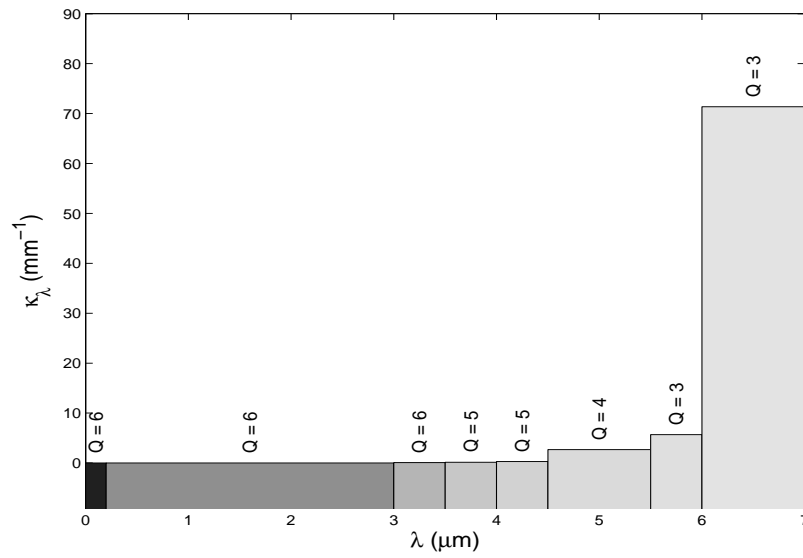


Figure 8: Eight-band model and the associated number of enrichments in the PUFEM.

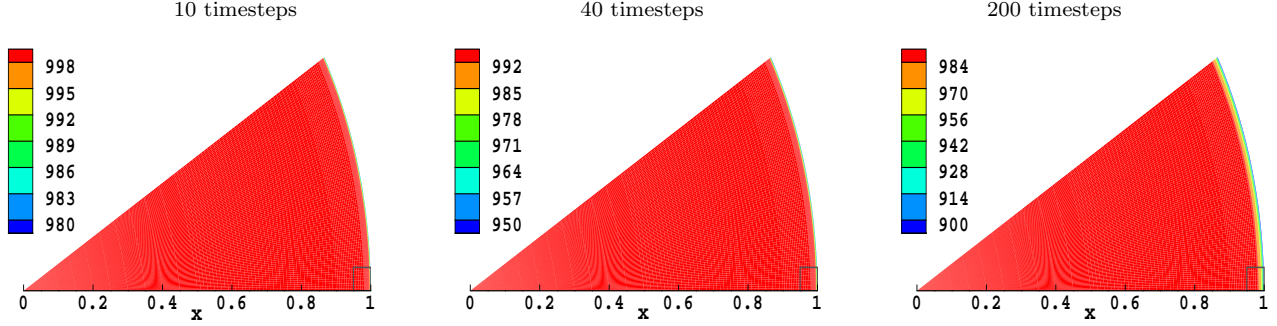


Figure 9: Temperature patterns obtained using the PUFEM at one element after 10 time steps (first column), 40 time steps (second column) and 200 time steps (third column). The square at the element corner is an indication of the zoom in Figure 10.

6.2 Glass cooling in a disc enclosure

In this test example we consider the annealing of a glass disc with unit radius. The thermodynamical and optical properties of the material are the same as in the previous example taken from Table 2. The objectives of this example are twofold: (i) to verify the performance of the PUFEM compared to the conventional FEM for the circular geometry, in terms of accuracy and efficiency when dealing with boundary layers, and (ii) to investigate a refined enrichment procedure in which the number of enrichment functions used, Q , varies with the eight frequencies bands. By considering this type of adaptive enrichment we expect to obtain a significant reduction in the overall computational cost since the number of degrees of freedom would vary for each band according to the associated absorption coefficient. We refer to this procedure as q -refinement, as opposed to the well-established h -refinement where the FEM mesh is adapted according to a measured error indicator. In the q -refinement, the PUFEM mesh remains the same during the simulation time and only the number of enrichment functions Q in (31) is allowed to vary for each frequency band. For the FEM simulations we consider two meshes (a coarse mesh referred to as FEMc and a fine mesh referred to as FEMf) which are presented in Figure 7. In this figure we also include the mesh used in our simulations using the PUFEM. We emphasise the extremely low number of elements and nodes listed in Figure 7 for the PUFEM mesh compared to both the coarse and fine FEM meshes.

It should be noted here that this glass cooling problem can also be solved as in the previous test example by retaining the same enrichments for the entire optical spectrum, *i.e.* the governing equations are solved without changing the enrichments for each frequency band. This is possible because the considered enrichment includes functions of a wide range of gradients from very steep to almost flat, which we have shown can be useful where no details are available on differences between radiation frequencies. Nevertheless, if these details are available then the PUFEM can be refined by defining an enrichment specific to each frequency band, such that functions with steep gradients are included in the enrichment only if the mean intensity, $\varphi^{(k)}$, develops high gradients for the frequency band $[\nu_k, \nu_{k+1})$. This refinement procedure can be significantly beneficial for radiative heat transfer models for which mean radiative intensities have to be computed for an optical spectrum with hundreds of frequency bands and only few of them require enrichment functions with steep gradients. Note that one of the key advantages in using the semi-implicit time integration scheme in (13) with the PUFEM formulation is to allow for different enrichments to be used for each frequency band as a mean intensity $\varphi^{(k)}$ with $k = 1, 2, \dots, 8$ can be solved independent of the other intensities. It is worth remarking that an h -refinement procedure with the FEM equivalent to the q -refinement, would require a different mesh to be assigned to each frequency band. This may be beneficial by reducing the computational costs of the solutions in some frequency bands. However, the interpolation needed to feed the radiation solution at all these bands back into the conduction is enough to eliminate any such benefit.

In the above mentioned series of tests it was observed that the mean radiative intensities $\varphi^{(7)}$ and $\varphi^{(8)}$

lead to a solution of a relatively uniform gradient over the computational domain. For the mean radiative intensities $\varphi^{(1)}$, $\varphi^{(2)}$ and $\varphi^{(3)}$, a sharp jump in the solution gradients is detected immediately on the domain boundary. As the domain releases its heat energy over time, this jump starts to dissipate, leading to a uniform gradient at late simulation times. This later phase is similar to the solutions obtained for the mean radiative intensities $\varphi^{(7)}$ and $\varphi^{(8)}$. In the other frequency bands, namely for the intensities $\varphi^{(4)}$, $\varphi^{(5)}$ and $\varphi^{(6)}$, the obtained results illustrate transient behavior in resolving moderate solution gradients between the above two forms. Regarding the conduction equation, the solution obtained for the temperature field exhibits similar behavior on the boundary as the solution obtained for the intensity $\varphi^{(1)}$ but with even sharper gradients at the early stage of the simulation. As the glass temperature approaches the ambient temperature, the heat released through radiation and conduction ceases and steady-state solutions are obtained. To summarize, the conduction equation starts at a steeper gradient compared to the solution of all the mean radiative intensities. Furthermore, the intensities $\varphi^{(4)}$ and $\varphi^{(8)}$ do not present steep gradients as $\varphi^{(1)}$ and $\varphi^{(3)}$. Therefore, the enrichment needed for the former bands is only a subset of the latter band enrichments which is in turn a subset of that of the conduction equation.

Next we present the numerical simulations using a q -refined PUFEM. The number of hyperbolic functions used to enrich the PUFEM solution space for solving the conduction equation is $Q = 7$. To solve the radiation equations for the mean intensities $\varphi^{(k)}$, with $k = 1, 2, \dots, 8$, the number of enrichment functions is $Q = 6$ for $\varphi^{(1)}$, $\varphi^{(2)}$ and $\varphi^{(3)}$, whereas $Q = 5$ for $\varphi^{(4)}$ and $\varphi^{(5)}$. This number is reduced to $Q = 4$ for $\varphi^{(6)}$ and $Q = 3$ for $\varphi^{(7)}$ and $\varphi^{(8)}$. In Figure ??? we summarize the distribution of the number of enrichment functions within the considered spectrum with eight frequency bands. As can be seen from this figure, a large number of enrichment functions is required for large values of absorption coefficients. This is expected as the diffusion coefficients in the simplified P_1 equations (12) are inversely proportional to the absorption coefficients ($\varepsilon^2/3\kappa_k$) and steeper boundary layers are expected for smaller diffusion coefficients. Note that due to the global nature of the enrichment, the saving in the computational cost is proportional to the saving in the number of enrichments since the total number of degrees of freedom equals the number of nodes multiplied by the number of enrichments. For instance, the total number of degrees of freedom is reduced by half when solving for $\varphi^{(7)}$ compared to $\varphi^{(1)}$ in our simulations. Thus, almost half of the computational cost in solving the radiation equation is saved when this refinement strategy is used compared to using a fixed number of enrichments $Q = 7$.

In Figure 9 we present snapshots of the temperature as recovered by the PUFEM on one element after 10, 40 and 200 time steps. In these simulations, the diffusion scale is $\varepsilon = 0.5$ and the time step size is $\Delta t = 10^{-7}$. It can be seen that, at early simulation times, in general the domain temperature remains uniform except in the boundary layer. To have a better insight on the boundary layer the square appearing at the lower right corner of the element in Figure 9 is zoomed. The zoomed region is shown in Figure 12 where the results obtained with the FEMc and FEMf are plotted alongside the PUFEM results. It is clear that both the FEM and the PUFEM capture the same cooling features in the disc. However, by focusing on the zooming displays it can be seen that the FEM on the coarse mesh exhibits non-physical oscillations at earlier time steps which are damped out as the simulation time progresses. These oscillations are reduced in the results obtained using FEMf but the PUFEM produces improved results for the time steps considered. The computed results for this test example demonstrate a more stable behavior with the PUFEM compared to FEMc and FEMf. Note that this accuracy in the PUFEM is achieved despite the fact that the total number of degrees of freedom for the PUFEM is only around 1% of that for FEMc.

In Figure 11 we illustrate the comparison, over a radial cross-section close to the domain boundary, of the temperature obtained using FEMc, FEMf and PUFEM at six different instants. The oscillations at the earlier simulation times after 10 and 40 time steps can clearly be seen on the FEMc results near the disc boundary. These oscillations, due to the failure of FEMc to resolve boundary layers at earlier simulation times, are damped out as the cooling time increases. For all simulation times, the PUFEM resolves the boundary layers without strong oscillations or excessive numerical dissipation and the temperature solutions closely match the FEMf results. At later times FEMc, FEMf and the PUFEM results coincide well.

To further examine the performance of the PUFEM we present in Figure 12 the radial cross-sections for the mean radiative intensities for six selected frequency bands after 10, 200 and 2000 time steps. The results

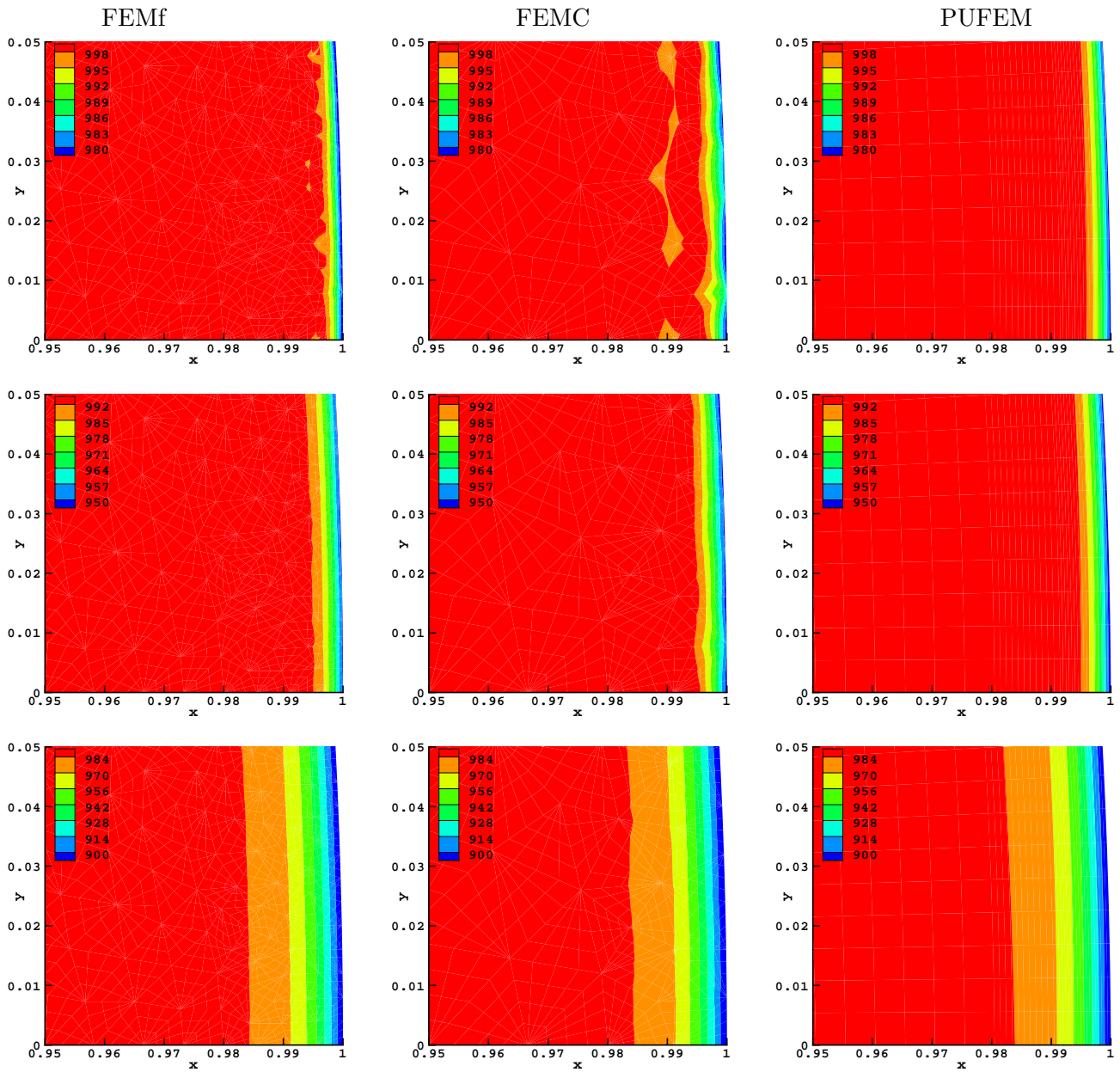


Figure 10: Temperature patterns obtained using FEMf (first column), FEMc (second column) and PUFEM (third column) after 10 time steps (first row), 40 time steps (second row) and 200 time steps (third row).

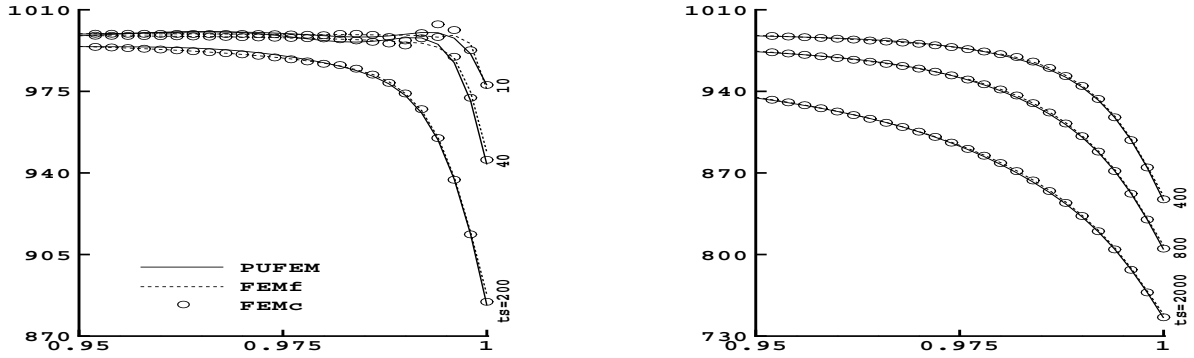


Figure 11: Comparison of radial cross-sections of the temperature obtained using FEMc, FEMf and PUFEM at six different instants after 10, 40, 200, 400, 800 and 2000 time steps.

obtained for $\varphi^{(5)}$ and $\varphi^{(8)}$ are not included in Figure 12 because they exhibit similar behavior to $\varphi^{(4)}$ and $\varphi^{(7)}$, respectively, but with different amplitudes. It is evident that the mean radiative intensities $\varphi^{(2)}$ and $\varphi^{(3)}$ develop steeper gradients than those associated with other frequency bands. Again spurious oscillations with different amplitudes are more pronounced in the FEMc results for the first three frequency bands after 10 and 200 time steps than in the PUFEM results. It should also be pointed out the largest mean radiative intensity is calculated for the last two frequency bands; compare, for example the values of $\varphi^{(7)}$ in Figure 12. These computed solutions for the mean radiative intensities $\varphi^{(7)}$ dominate the other solutions in the remaining frequency bands. As a consequence, the smooth boundary layers in $\varphi^{(7)}$ may introduce stabilizing effects in the considered radiative heat transfer problem. As mentioned earlier, the pattern described above when refining the enrichment can be seen in Figure 11 and Figure 12 in the steeper gradient associated with the conduction as well as the mean radiative intensities $\varphi^{(1)}$, $\varphi^{(2)}$ and $\varphi^{(3)}$. A relatively flat gradient can be seen in the intensities $\varphi^{(7)}$ and $\varphi^{(8)}$. The PUFEM performs very satisfactorily for this frequency-dependent coupled problem since it does not diffuse the moving fronts and no spurious oscillations have been detected near steep gradients of the temperature field and radiative intensities in the computational domain.

7 Conclusions

The solution of conduction radiation problems at early time steps is a challenging task even when very fine meshes are used. The shock of temperature change at the first time steps seems to move forward in the time domain up to a certain time. Requiring only a small fraction of the number of degrees of freedom required with the FEM, the PUFEM shows better stability compared to that observed with the FEM. The advantages of the PUFEM optimization exploit this reduction in the number of degrees of freedom further for problems with tens of frequency bands, such as those found in industrially relevant simulations. In general as it is observed in the second test case and for the cross section of the domain the FEM on fine meshes and the PUFEM leads to similar results with the advantages that the PUFEM shows a more stable behaviour and the for a large reduction in the computational costs. The PUFEM and the FEM shows differences at early time steps and at the domain edges. An optimized PUFEM approach is presented. It is found that the enrichment needed for the radiation equation is only a subset of that of the conduction equation. Furthermore the bands of [lower frequencies is enriched with a subset of the higher frequencies bands](#). The time implicit procedure enables multiple enrichment for different frequency bands. This optimization can be very useful if hundreds of frequency bands are needed. Based on the solution pattern observed for this optical regime a so called q -refinement procedure is proposed. It is found that this procedure is useful.

The partition of unity finite element method introduced for conduction radiation problems in our earlier work [] has been adopted here for glass cooling problem. The technique is applied to a physical model of

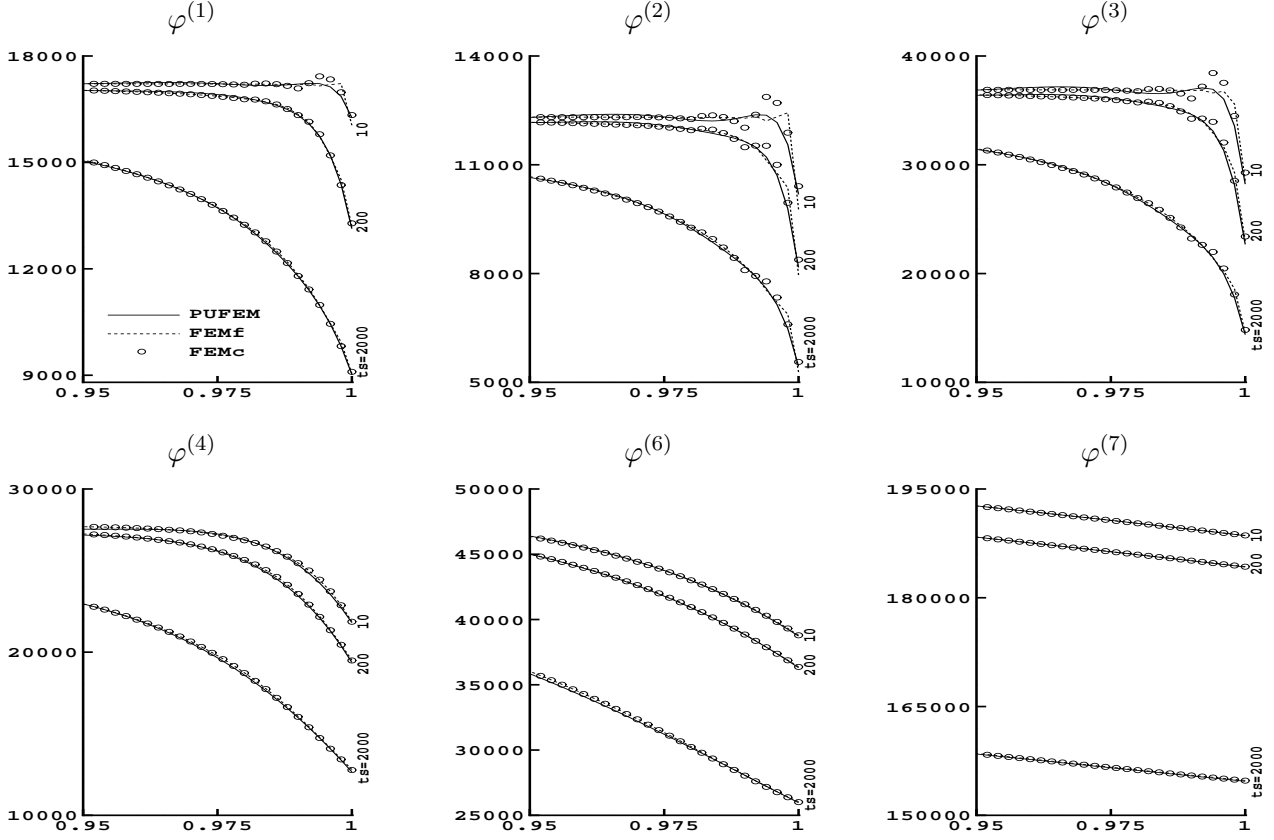


Figure 12: Comparison of radial cross-sections of the mean radiative intensities obtained using FEMc, FEMf and PUFEM at three different instants after 10, 200 and 2000 time steps.

glass that is published in [] to allow accurate simulation of the cooling process at a significantly reduced computational cost compared to other numerical methods including the finite differences and the full radiative transfer. The study highlight the performance of the PUFEM in recovering the solution on the boundary layer. Two numerical test cases are shown where the PUFEM results are compared to the h -version FEM method. An optimization strategy of the PUFEM method is discussed in the second example. The time implicit procedure enables multiple enrichment for different frequency bands.

An optimized PUFEM approach is presented. It is found that the enrichment needed for the radiation equation is only a subset of that of the conduction equation. Furthermore the bands of **lower frequencies is enriched with a subset of the higher frequencies bands**. The time implicit procedure enables multiple enrichment for different frequency bands. This optimization can be very useful if hundreds of frequency bands are needed. Based on the solution pattern observed for this optical regime a so called q -refinement procedure is proposed. It is found that this procedure is useful. We study this industrial model and apply a refined PUFEM procedure to it.

because the main challenge in this problem is related to the steep gradient in the boundary layers it is found that adding steep gradient enrichment circumvent any need to mesh refinement. Other than these steep gradient the solution can be very trivial and can be recovered with a very coarse finite element mesh. We show this.